Heat Mass Transfer (2008) 44:1015–1023
DOI 10.1007/s00231-007-0316-x

ORIGINAL

Measurement of acoustic velocity in the stack of a thermoacoustic refrigerator using particle image velocimetry

**Arganthaël Berson · Marc Michard ·
Philippe Blanc-Benon**

Received: 1 June 2007 / Accepted: 3 July 2007 / Published online: 8 August 2007

Abstract Thermoacoustic refrigeration systems generate cooling power from a high-amplitude acoustic standing wave. There has recently been a growing interest in this technology because of its simple and robust architecture and its use of environmentally safe gases. With the prospect of commercialization, it is necessary to enhance the efficiency of thermoacoustic cooling systems and more particularly of some of their components such as the heat exchangers. The characterization of the flow field at the end of the stack plates is a crucial step for the understanding and optimization of heat transfer between the stack and the heat exchangers. In this study, a specific particle image velocimetry measurement is performed inside a thermoacoustic refrigerator. Acoustic velocity is measured using synchronization and phase-averaging. The measurement method is validated inside a void resonator by successfully comparing experimental data with an acoustic plane wave model. Velocity is measured inside the oscillating boundary layers, between the plates of the stack, and compared to a linear model. The flow behind the stack is characterized, and it shows the generation of symmetric pairs of counter-rotating vortices at the end of the stack plates at low acoustic pressure level. As the acoustic pressure level increases, detachment of the vortices and symmetry breaking are observed.

A. Berson (✉) · M. Michard · P. Blanc-Benon
LMFA – UMR CNRS 5509, Ecole Centrale de Lyon,
36 Av. Guy de Collongue, Ecully Cedex 69134, France
e-mail: arganthael.berson@ec-lyon.fr
URL: http://www.acoustique.ec-lyon.fr

1 Introduction

The thermoacoustic effect of interest in thermoacoustic refrigeration results from the interaction of an acoustic wave and a solid wall. Under adequate conditions, a high amplitude standing wave creates a temperature gradient along a stack of plates. A heat flux appears then from the cold side to the hot side of the plates. This heat flux results from the adequate phasing between the compression–expansion cycle and the oscillatory motion that is imposed on a fluid particle by the acoustic standing wave, as described by Swift [25] and shown in Fig. 1. As it moves towards the pressure antinode, the particle heats up because of compression (a). It becomes hotter than the plate and then gives heat to it (b). As it moves back to the velocity antinode, the particle expands (c). It cools down and since it becomes cooler than the plate, it gains heat from it (d). And the cycle starts again.

Thermoacoustic refrigeration, which is based on this effect, is a promising alternative to the traditional vapor-compression technology. It is free of harmful refrigerants and has a simple architecture, with few mechanical moving parts, which potentially allows the development of miniature devices. Theoretically, a standing-wave thermoacoustic refrigerator can achieve efficiencies of 40–50 % of Carnot's efficiency [29]. However, the systems built so far have a poor efficiency compared to the efficiency that is theoretically achievable [22]. A better understanding of the flow field around the components of a thermoacoustic refrigerator is crucial for increasing the efficiency of such systems.

It is well known that linear thermoacoustics [24, 25] is reliable at low amplitude acoustic pressure. However, industrial applications usually require a high acoustic pressure level inside the resonator. At high amplitude

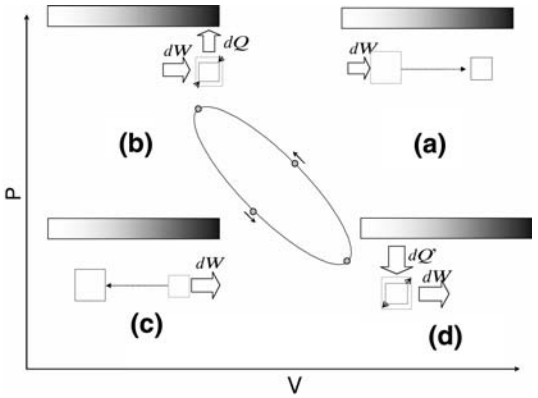

Fig. 1 Diagram of pressure versus velocity of the thermoacoustic cycle for a heat pump with schematic drawings of heat exchanges between a fluid particle and a stack plate. **a** The particle moves towards the pressure antinode and heats up because of acoustic compression. **b** The particle is hotter than the stack plate and gives heat to it. **c** The particle moves back to the velocity antinode and expands. **d** The particle cools down because of acoustic expansion and is cooler than the plate. The particle gains heat from the plate

($DR = P_{ac}/P_m > 3\%$, the drive ratio *DR* being the ratio of acoustic pressure level and mean pressure), nonlinear effects such as streaming appear and edge effects become more important. These local phenomena are expected to influence strongly the overall efficiency of thermoacoustic systems. The study of the coupling between the stack and heat exchangers is also important for the optimization of the interfacing between the refrigerator and the ambient. Several numerical calculations recently addressed the modelling of the flow field inside a thermoacoustic refrigerator. Cao et al. [8] were the first to simulate thermoacoustics over a 1D-isothermal plate, solving the full 2D-Navier–Stokes equations. Worlikar and Knio [30] performed a computation of the flow at the edges of a 2D-plate, while Besnoin and Knio [3] obtained the flow field over the same plate coupled with a heat exchanger. The last two simulations were based on a low-Mach-number approximation. Direct computations of the full 2D-Navier–Stokes equations, with specific boundary conditions that take into account the reflection of the wave at the end of the resonator for a better representation of the acoustic field, were performed for the cases of a 1D-isothermal-plate [14, 18], a 1D-plate coupled with heat exchangers [17] and a 2D-plate [16].

Experimental studies of thermoacoustic systems mainly focus on performance measurements, such as in Poese and Garrett [23] or Paek et al. [21]. Little experimental work has been done, however, to visualize flow structures and measure the unsteady velocity fields in thermoacoustics. The flow field in a thermoacoustic refrigerator should preferably be investigated using optical methods that are non-intrusive. Herman et al. [12] used holographic interferometry for the visualization of the flow near the stack plates of a model of thermoacoustic refrigerator. The same authors [28] also used smoke visualization to get better insight of the flow field before performing thermal measurements. They highlighted the presence of a vortex at the edge of a stack plate, but no precise description of the phenomenon was given. Taylor [26] was the first to measure the acoustic velocity in an acoustic resonator, using laser Doppler anemometry (LDA). This local measurement technique, that yields data only for a single point in the measurement volume, has also been used by Bailliet et al. [1] and Biwa et al. [4] to measure the acoustic power flow in a thermoacoustic resonator, and by Thompson and Atchley [27] for streaming measurements. In the present study, particle image velocimetry (PIV) will be preferred to LDA since it allows to obtain velocity data over a large area. Humphreys et al. [13] have performed PIV measurements in an impedance tube. Hann and Greated [11] developed an unconventional method of extracting acoustic velocity in an acoustic standing wave from the spectrum of multiply exposed PIV images. A review of the use of LDA and PIV to measure acoustic and streaming velocities is proposed by Campbell et al. [7].

The experimental work presented here addresses the characterization of the flow inside a thermoacoustic refrigerator using PIV. The experimental setup is described in Sect. 2. Also, in this section, the measurement technique is validated by comparing the velocity fields obtained in the resonator without stack to a simple plane wave model. Section 3 presents the results. The oscillating boundary layers between two plates of the stack are investigated, showing good agreement with an analytical solution. The generation of vortices at the edges of the stack plates is precisely described. At high acoustic pressure level, we observe for the first time the detachment of vortices and the symmetry breaking of the vortex street.

2 Experimental setup

2.1 The thermoacoustic refrigerator

A schematic view of the thermoacoustic refrigerator used in the present study is given in Fig. 2. It is made of a closed acoustic resonator with a driver at one end and a stack of flat parallel plates inside. The length of the resonator is 86 cm and its cross-sectional area is 80 × 80 mm^2. The walls of the resonator are made of transparent plexiglas. The driver is a common high fidelity loudspeaker delivering a monotonic sound at the tube resonance frequency $f_0 = 214$ Hz (half-wavelength resonator). The acoustic pressure level inside the resonator reaches up to 2,000 Pa. The working gas is air at atmospheric pressure ($P_m = 1$

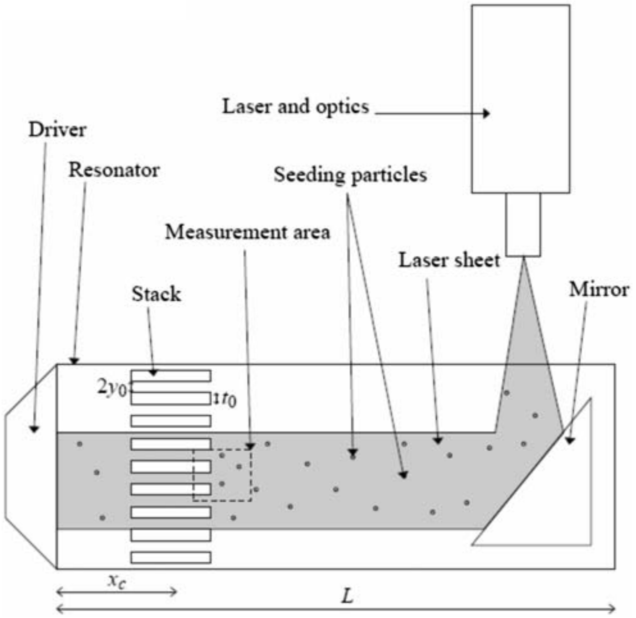

Fig. 2 Schematic view of the thermoacoustic refrigerator and optical setup for PIV measurements

atm). Acoustic pressure is monitored by a 1/4 in. Bruel & Kjaer microphone placed a few centimeters away from the loudspeaker at the pressure antinode. The plates of the stack are made of glass, which is a non-conducting material (k_s = 1.05 W/m K). The thickness of the plates is t_0 = 1 mm and the interplate spacing is $2y_0$ = 1 mm (blockage ratio:$BR = 2y_0/(2y_0 + t_0) = 0.5$). The plates are l = 25 mm long. The center of the stack is located x_c = 21.5 cm away from the driver, where the amplitudes of both pressure and velocity fluctuations are high enough for the thermoacoustic effect to take place.

The specific features of PIV impose technical constraints on the design of the refrigerator. The refrigerator described above is not optimized to achieve high thermal efficiency. The length scales for the thermoacoustic effect are the thicknesses of the thermal and viscous oscillating boundary layers, defined respectively by $\delta_\alpha = \sqrt{2\alpha/\omega}$ and $\delta_v = \sqrt{2v/\omega}$, where α is the thermal diffusivity of the gas, v its kinematic viscosity, and ω the angular frequency of the oscillation. The ratio of these two quantities is given by $\delta_v/\delta_\alpha = \sqrt{\sigma}, \sigma$ being the Prandtl number of the working gas. Characteristic dimensions of the present system are summarized in Table 1. In order to minimize viscous losses, an optimized design would require the use of a low Prandtl number gas as a working fluid. Also, as for the optimization of stack performances, Swift [25] recommends the spacing between the plates to be approximately twice the thermal penetration depth δ_α. Although the present setup is not thermally optimized, conclusions presented here hold for systems designed for high performances.

Table 1 Characteristic dimensions of the thermoacoustic refrigerator

f (Hz)	214	$2y_0$ (mm)	1
L (m)	0.86	t_0 (mm)	1
x_c (m)	0.215	δ_α (mm)	0.18
l (m)	0.025	δ_v (mm)	0.15
P_m (atm)	1	σ	0.7

2.2 The PIV measuring system

2.2.1 Optical setup

The optical setup is represented in Fig. 2. The camera is a LaVision FlowMaster 3^{TM} with a 1,280 × 1,024 pix^2 (8.6 × 6.9 mm^2) CCD sensor. Measurement fields of minimum area 11 × 9 mm^2 are obtained with a Nikon^{TM} 60 mm lens and extension tubes. The working distance is approximately 10 cm from the measurement field and magnification is estimated to be 0.77. The camera is placed perpendicular to the direction of oscillations. The laser sheet is generated by a dual-resonator Nd:YAG laser with a wavelength of 532 nm, and combined with a cylindrical lens. The time between 2 pulses is 52 µs for 500 Pa, 26 µs for 1,000 and 1,500 Pa, and 13 µs for 2,000 Pa. It has to be small enough compared to the acoustic period (T = 4.6 ms) for velocity variations to be negligible between two laser pulses. Close to flow reversal, when time derivative of acoustic velocity is at its maximum, the error due to velocity variations between two laser pulses is estimated to be 6.6 cm s^{-1} for 500, 1,000 and 2,000 Pa, and 9.8 cm s^{-1} for 1,500 Pa, for measurements made at x_c = 22.75 cm. These values correspond to 7% of the velocity amplitude at 500 Pa, 3.5 % at 1,000 and 1,500 Pa, and 1.75 % at 2,000 Pa. A small and thin mirror of dimensions 90 × 5 mm^2, with a 45°-angle with respect to the direction of oscillations, is placed inside the resonator to reflect the laser sheet and create the measurement plane perpendicular to the plates of the stack and to the optical axis of the camera. The laser does not illuminate the edges of the stack directly so that there are no unwanted reflections on the stack plates. The mirror is located far from the stack, inside the opposite half of the resonator, and since its dimensions are small with respect to the acoustic wavelength, it does not disturb the acoustic wave.

2.2.2 Particle seeding

The measurement plane is seeded with paraffin oil smoke generated by a commercial smoke machine. The smoke is filtered to eliminate large particles. The diameter of the particles ranges from 1 to 4 µm. According to the characteristics of the optical system and for an aperture of

4 mm, the diameter of a particle image on the sensor is approximately 5 pix which satisfies the requirements of the PIV software. The smoke is fed inside the resonator through a capillary tube flush-mounted in a wall, near the measurement area. Another flush-mounted capillary tube is placed further on the wall. Its other end is immersed in water in order to maintain constant pressure inside the resonator during smoke injection. Smoke is injected before turning the loudspeaker on. Acoustic oscillations make the seeding homogeneous and measurements can be performed.

Since we are interested in the characteristics of an unsteady flow, it is necessary to verify that particles follow the flow for the frequency range of interest. This will ensure that the measured velocity is in good agreement with the actual flow field. As proposed in the review by Melling [19], we solve the equation of motion of a seeding particle. Considering that the particle density is greater than the fluid density $\rho_p/\rho_f \gg 1$, this equation reduces in our case to

$$\rho_p \frac{\pi d_p^3}{6} \frac{dU_p}{dt} = -3\pi\mu d_p (U_p - U_f), \tag{1}$$

where ρ_p, μ, and d_p are the density, dynamic viscosity and diameter of the seeding particle, respectively. U_f and U_p are instantaneous velocities of the fluid and seeding particle, respectively. The ratio $\eta = U_p/U_f$ of these two velocities is obtained from the solution of Eq. 1. Assuming that particles follow the flow for $\eta > 0.99$, the maximum acceptable diameter for a particle of paraffin oil smoke is 6.38 μm at the frequency of interest ($f_0 = 214$ Hz). It is greater than the size of the particles introduced into the resonator. Hence, we conclude that the use of paraffin oil smoke is appropriate for PIV measurements in the setup presented here.

2.2.3 *Data acquisition and processing*

The maximum repetition rate of the camera for PIV measurements is $f_{cam} = 2$ Hz, which is below the frequency of oscillation ($f_0 = 214$ Hz). This limitation is overcome using phase averaging. Acoustic velocity being periodical, PIV image acquisition is phase-locked with the voltage feeding the loudspeaker using a TTL triggering signal delivered by the signal generator. A time lag τ between TTL signal and the time when both camera and laser are triggered is defined in the software. By adjusting τ, an acoustic cycle is subdivided in 16 equally spaced phases. We define the initial phase (0°) as the time when velocity is zero and when the fluid flows out of the cold side of the stack during the following half period. Fifty instantaneous velocity fields are measured for each phase, and averaged in order to obtain a phase-averaged velocity field.

Velocity fields are processed from the images with the commercial system Lavision Davis 7.0™. Multiple iterations with window shift and decreasing window size ensure a high spatial resolution with low signal-to-noise ratio. As shown by Berson et al. [2], spatial resolution is a limiting parameter for a good estimation of space derivatives that are used in the calculation of quantities such as vorticity or viscous dissipation. The size of the final interrogation windows is 16 × 16 pix^2 with 50 % overlap, leading to a spatial resolution of 70 μm for a measurement area of 11 × 9 mm^2.

The z-component of the vorticity vector $\Omega_2 = (\partial v/\mathrm{d}x - \partial u/\mathrm{d}y)/2$ is calculated. The Γ_2 function is also computed to detect vortex boundaries. Let M be a point of the plane, Γ_2 is defined by:

$$\Gamma_2(\mathbf{x}) = \frac{1}{S} \iint_{M' \in S} \sin\theta \,\mathrm{d}x_i' \mathrm{d}x_j', \tag{2}$$

where S is a disc of center M. θ is the angle between $\mathbf{x}' - \mathbf{x}$ and $\mathbf{u}(M') - \mathbf{u}(M')$, M' being a point inside S with coordinates $\mathbf{x}'$, and $\mathbf{u}(M)$ is the velocity at coordinate M. The radius of S is four times the spatial resolution. Subscripts i and j refer to the vector components in the plane. $|\Gamma_2|$ has values between $2/\pi$ and 1 when the flow is locally dominated by rotation. Γ_2 function is a non-dimensional quantity based on the topological properties of the flow rather than on its intensity. Thus, it is a powerful tool to detect vortex boundaries in a strongly inhomogeneous flow such as the present one. More details about Γ_2 function can be found in Graftieaux et al. [10].

2.3 Acoustic velocity in the resonator without stack: validation of the measurements

The experimental setup presented here has already been validated by Duffourd [9]. In this section, we operate in the resonator of the thermoacoustic refrigerator without stack. Thus, we consider the resonator as a closed tube with a piston-like source at the $x = 0$ end. The driver delivers a sinusoidal excitation at the tube resonance frequency $f_0 = 214$ Hz. In this configuration, an acoustic standing wave is formed in the resonator. At this range of frequencies, no transversal modes are excited and the acoustic wave is plane. This means that velocity remains constant in a cross-section of the tube (except within the viscous boundary layer close to the walls). The velocity in a cross-section of abscissa x can be deduced from the maximum acoustic pressure inside the resonator as

$$U(x,t) = U(x)\sin(\omega t) = \frac{P_{ac}}{\rho_0 c_0} \sin(kx)\sin(\omega t), \tag{3}$$

where P_{ac} is the maximum acoustic pressure in the resonator, ρ_0 is the density of air, c_0 is the celerity of sound in air, $k = \omega/c_0$ is the acoustic wavenumber and t is time. The maximum acoustic pressure inside the tube is 1,500 Pa. At this level of acoustic pressure, harmonics appear but remain quite low (second harmonic is no more than a few percents of the fundamental). This introduces only a slight error when data are compared to the model without harmonics. Duffourd [9] extended the model to take into account higher harmonics, and found a good agreement with experimental data.

The measurement area is located 35 cm away from the driver and spatial resolution is 70 µm. Velocity at x = 35 cm is plotted in Fig. 3 for each measured phase of the acoustic cycle. It is in good agreement with the velocity calculated from the maximum acoustic pressure, using Eq. 3. The maximum error between experimental data and the model is 0.13 m s^{-1}, or 3.7 % of the maximum velocity. It is of the same order as the error made because of velocity variations between two laser pulses. Velocity fields are also presented in Fig. 3, corresponding to two different phases. The velocity is uniform along the transversal direction y, which validates the plane wave assumption.

To conclude, it is demonstrated that acoustic velocities can be measured accurately using PIV. In a void resonator, measurements compare well with a simple model of a plane acoustic standing wave. In the next sections, results for oscillating boundary layers between two plates of the stack and for the flow near the stack edges will be presented.

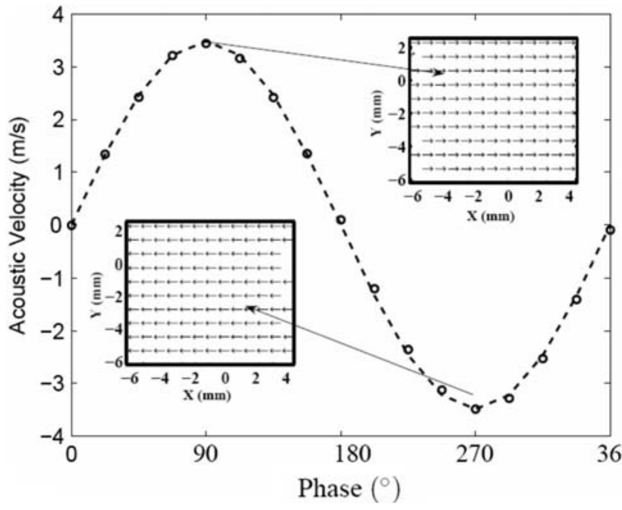

Fig. 3 Velocity averaged over a cross-section of the resonator (x = 35 cm) for different phases of a period of oscillation. *Open circle* experimental datapoints. *Dashed lines* plane acoustic standing wave model (P_{ac} = 1500 Pa)

3 Results

3.1 Oscillating boundary layers

The characterization of oscillating boundary layers inside the stack is crucial for the understanding of the thermoacoustic effect. Indeed, the thermoacoustic effect takes place in the viscous and thermal boundary layers along the stack plates, where there is an adequate phasing between velocity and temperature fluctuations.

We measure the oscillatory flow between two plates of the stack. Equation 4, that is derived from the linearized momentum equation of the viscous fluid [25], gives the oscillating velocity between two parallel plates.

$$U(x,y) = \frac{\langle U\rangle(x)}{1-f_v}\left(1-\frac{\cosh\left[(1+i)y/\delta_v\right]}{\cosh\left[(1+i)y_0/\delta_v\right]}\right), \tag{4}$$

where $\langle U\rangle$ (x) is the acoustic velocity integrated over the height of a channel, and the thermoviscous function f_v is defined as $f_v = \tanh[(1+i)y/\delta_v]/[(1+i)y_0/\delta_v]$.

The phase-averaged velocity profiles measured in a stack channel are given in Fig. 4, for eight phases of the acoustic period, and two acoustic pressure levels: 500 and 2,000 Pa. Measurements are performed inside the cross-section of a channel located 4.8 mm away from the cold edges of the plates. The centre of the stack is placed at x_c = 21.5 cm. Both end points of each velocity profile belong to the plates. They have zero velocity and are plotted for reference. Spatial resolution is 80 µm. A precise description of the flow close to the wall would require a better spatial resolution, but this is beyond the scope of this paper.

The flow inside the channel is laminar and it is strongly influenced by viscous effects. Indeed, the viscous boundary layers occupy no less than approximately one third of the space between two plates. When the sign of the acoustic velocity changes (at $\Phi = 0°$ and $\Phi = 180°$), flow reversal appears first in the viscous boundary layer, where the flow has less inertia. Hence, the fluid in the middle of the channel and the fluid close to the plates flow in opposite ways. These measurements are in accordance with the model described by Eq. 4.

Comparisons between velocity profiles measured with PIV and theoretical velocity profiles calculated from Eq. 4 show good qualitative agreement. At low acoustic pressure level (500 Pa), discrepancies between the measurements and the linear model are within experimental error. However, the linear model is less accurate at higher level (2,000 Pa). This is likely to be due to nonlinearities that start to appear as acoustic load increases. At even higher acoustic pressure level, one should expect effects such as streaming or turbulent structures to appear inside these boundary layers. This will affect the efficiency of the system.

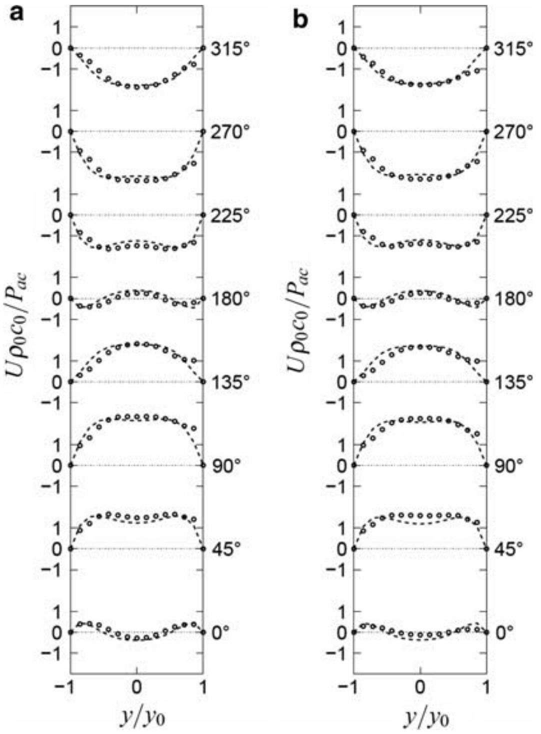

Fig. 4 Velocity profiles inside a channel of the stack, for different phases during an acoustic cycle, at P_{ac} = 500 Pa (**a**) and P_{ac} = 2,000 Pa (**b**). Velocity is normalized by the maximum acoustic velocity amplitude in the resonator. Position inside the channel is normalized by half the height of the channel. The center of the stack is 21.5 cm away from the driver. Velocities are measured 4.8 mm away from the cold end of the stack. Phases 0°, 45°, 90°, 135°, 180°, 225°, 270°, and 315° are represented from bottom to top. *Open circle* experimental datapoints. *Dashed lines* linear model derived from Eq. 4

3.2 Velocity fields at the edges of the stack plates

Blanc-Benon and Marx [5] have shown that the topology of the flow behind the stack has a strong influence on the heat flux close to the edges of the stack plates. The aerodynamic field behind the stack depends on its geometry. Experiments have been performed previously with this experimental setup for different stack geometries, at low acoustic pressure level ($P_{ac} \leq$ 1,500 Pa), and compared to numerical simulations [6, 15]. In this paper we focus on the stack described in Sect. 2.1, whose blockage is high and whose plates are thick. The center of the stack is located at x_c = 21.5 cm, and spatial resolution of the measurements is 85 µm.

Close-ups of velocity fields at the edge of the stack plates, at P_{ac} = 500 Pa are given in Fig. 5 for selected time instants during an acoustic cycle. In this section, we focus on the cold side of the stack, but the same analysis remains valid for the hot side. During the phases when the fluid flows out of the stack (from phases 0° to 180°), the fluid rolls up around the sharp edges of the stack plates, due to flow separation. This mechanism leads to the generation of two counter-rotating vortices behind each stack plate. These vortices are symmetric and remain attached to the edges of the stack plates. At phases 202.5° and 225°, the fluid is sucked back between the plates. The persistence of the formerly generated vortices makes the flow slightly rotational, and creates areas of low velocity just behind the channel. From phases 247.5° to 360°, the fluid enters the channel, flowing around the plate edges. Fluid velocity is higher within the channel than outside because of the blockage created by the presence of the stack in the resonator.

At higher acoustic pressure level, the topology of the flow is different. Figure 6 shows vorticity fields and Γ_2 iso-lines behind stack plates for eight different phases of an acoustic period. Figure 6e helps to situate the phases on an acoustic period. Acoustic pressure level is P_{ac} = 2,000 Pa. During the first quarter of an acoustic cycle (from phases 0° to 90°), the fluid flows out of the cold side of the stack and velocity magnitude increases. Similarly to what happens at lower pressure, two counter-rotating vortices are generated from the edges of the stack plates, due to flow separation. As the flow decelerates (from phases 90° to 180°), vortices are shed away from the stack edges. We observe that the pairs of counter-rotating structures lose their symmetry so that, at flow reversal (phase 180°), an asymmetric street of vortices appears behind the stack. Vortical structures remain present during the following phase (phase 202.5°), when the fluid starts flowing back into the cold side of the stack. Eventually, until the end of the entering phase (from phases 225° to 360°), we observe high vorticity solely inside the oscillating boundary layers along the stack plates.

Detachment of vortices and loss of symmetry appear at high acoustic pressure levels only. Figure 7 shows normalized vorticity fields and Γ_2 iso-lines close to the cold end of the stack, at flow reversal (phase 180°), for four different acoustic pressure levels: P_{ac} = 500 Pa, P_{ac} = 1,000 Pa, P_{ac} = 1,500 Pa, and P_{ac} = 2,000 Pa. The corresponding acoustic Reynolds numbers (Re_{δ_ν}) are calculated according to Eq. 5. Numerical values are given in Table 2.

$$Re_{\delta_\nu} = \sqrt{2}\frac{U(x)}{BR}\frac{\delta_\nu}{\nu}. \tag{5}$$

In Fig. 7, we observe that until $Re_{\delta_\nu} = 51$, pairs of counter-rotating vortices remain symmetrically attached to the stack edges during the whole time when fluid flows out of the cold side of the stack (from phases 0° to 180°). Vortices detach from the stack edges for $Re_{\delta_\nu} \geq 76$. Merkli and Thomann [20] found that onset of turbulence occurs at $Re_{\delta_\nu} = 400$ in the Stokes boundary layers of an oscillating flow. At P_{ac} = 2,000 Pa, Re_{δ_ν} is approximately four times lower than the

Fig. 5 Close-ups of velocity fields at the cold edge of the stack, at $P_{ac} = 500$ Pa. The following phases are represented: **a** 0°, **b** 22.5°, **c** 45°, **d** 67.5°, **e** 90°, **f** 112.5°, **g** 135°, **h** 157.5°, **i** 180°, **j** 202.5°, **k** 225°, **l** 247.5°, **m** 270°, **n** 292.5°, **o** 315°, **p** 337.5° and **q** 360°. For the sake of clarity, the velocity field is undersampled

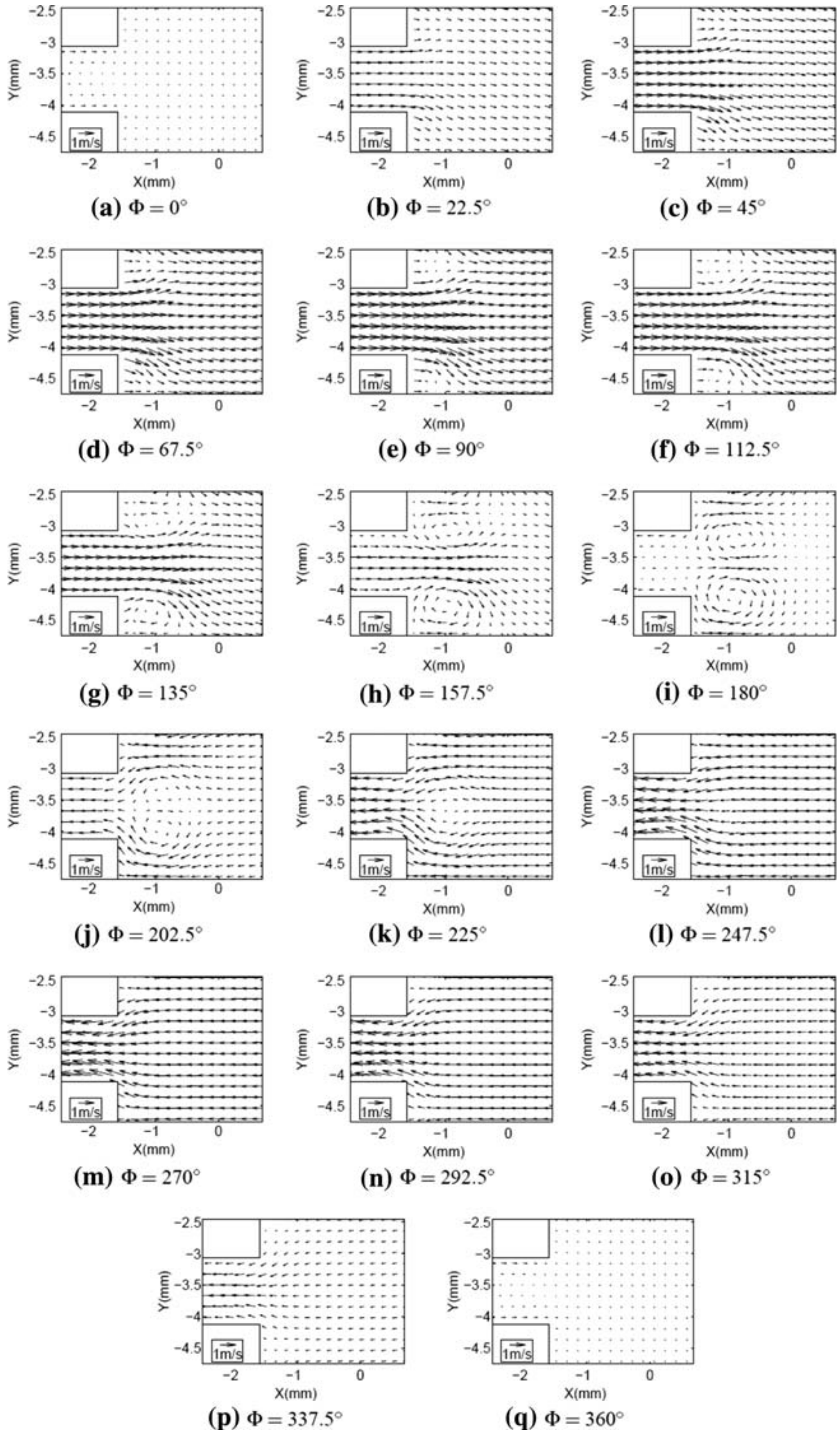

(a) $\Phi = 0°$ **(b)** $\Phi = 22.5°$ **(c)** $\Phi = 45°$

(d) $\Phi = 67.5°$ **(e)** $\Phi = 90°$ **(f)** $\Phi = 112.5°$

(g) $\Phi = 135°$ **(h)** $\Phi = 157.5°$ **(i)** $\Phi = 180°$

(j) $\Phi = 202.5°$ **(k)** $\Phi = 225°$ **(l)** $\Phi = 247.5°$

(m) $\Phi = 270°$ **(n)** $\Phi = 292.5°$ **(o)** $\Phi = 315°$

(p) $\Phi = 337.5°$ **(q)** $\Phi = 360°$

critical Reynolds number, so it is clear that the detachment of vortices is not related to the transition of the flow towards turbulence. We remark that, regardless of the acoustic pressure level, the vortex street never extends further than two acoustic displacements ($2d_{ac} = 2U/\omega$) away from the stack edges. Two acoustic displacements are the distance a particle can travel during an acoustic cycle. Thus, it is likely that, at low Reynolds number, the first vortex is not convected sufficiently far away from the stack edges for it to detach and for a second vortex to appear. Measurements at higher pressure level, showing more vortices in the vortex street, should be performed to verify this assumption.

4 Conclusion

Measurements are performed in a standing-wave thermoacoustic refrigerator using PIV. A specific PIV method is

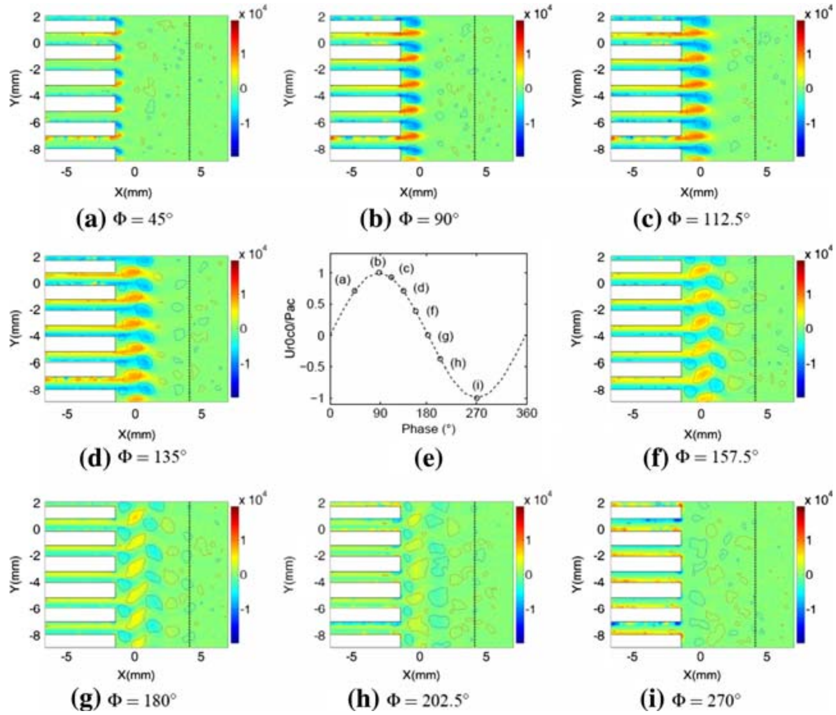

(a) $\Phi = 45°$ (b) $\Phi = 90°$ (c) $\Phi = 112.5°$

(d) $\Phi = 135°$ (e) (f) $\Phi = 157.5°$

(g) $\Phi = 180°$ (h) $\Phi = 202.5°$ (i) $\Phi = 270°$

Fig. 6 Vorticity fields (in s^{-1}) and iso-lines of $\mid \Gamma_2 \mid = 2/\pi$ at the cold edge of the stack, at P_{ac} = 2,000 Pa. The following phases are represented: **a** 45°, **b** 90°, **c** 112.5°, **d** 135°, **f** 157.5°, **g** 180°, **h** 202.5° and **i** 270°. The *dashed line* represents the distance $2d_{ac}$ away from the stack edges. Positions of the phases along the acoustic cycle are represented on the plot of normalized acoustic velocity versus time given in (**e**)

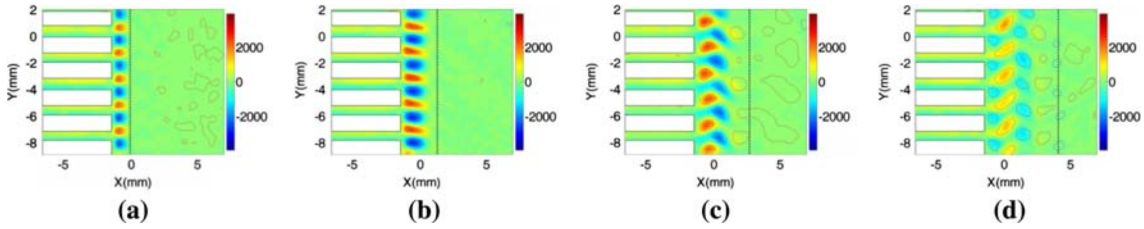

(a) (b) (c) (d)

Fig. 7 Normalized vorticity fields ($\Omega_2\ \rho_0\ c_0^2/P_{ac} f_{osc}$) and iso-lines of $\mid \Gamma_2 \mid = 2/\pi$ at the cold edge of the stack, at phase 180°, and for different acoustic pressure levels: **a** P_{ac} = 500 Pa, **b** P_{ac} = 1,000 Pa, **c** P_{ac} = 1,500 Pa, and **d** P_{ac} = 2,000 Pa. The *dashed line* represents the distance $2d_{ac}$ away from the stack edges

Table 2 Magnitude of acoustic velocity, acoustic displacement and acoustic Reynolds numbers inside the channels, calculated at the location of the cold side of the stack x = 22–75 mm

P_{ac} (Pa)	$U(x$ = 22.75 cm) (m s^{-1})	$2d_{ac}$ (x = 22.75 cm) (mm)	Re_{δ_ν}
500	0.94	1.4	26
1,000	1.88	2.8	51
1,500	2.81	4.2	76
2,000	3.75	5.6	102

developed, using synchronization and phase-averaging for the measurements of acoustic velocities. The method is validated in an acoustic resonator (without stack) by successfully comparing experimental data to a simple plane wave model. The flow inside the channels of the stack is studied and shows good quantitative agreement at P_{ac} = 500 Pa. The measuring method is validated and shows the limitations of the linear model at higher acoustic pressure level, when nonlinearities appear. Acoustic velocity fields behind the stack plates are characterized. Vortices appear during the half period of the acoustic cycle when the fluid flows out of the stack. At low acoustic pressure level, counter-rotating vortices are generated at the edges of the plates. They are symmetrical and remain attached to the plates. With increasing acoustic pressure level, structures detach and create an asymmetric street of vortices. Regardless of the pressure level, vortices are not shed further than two acoustic displacements away from the stack edges. In future studies, higher acoustic pressure levels will be required for a more precise description of the mechanisms of vortex shedding behind the stack plates.

Acknowledgements Part of this work was supported by ANR (project MicroThermoAc NT051_42101). The authors are also grateful to N. Grosjean, J.-M. Perrin and Ch. Nicot for their technical assistance during all the stages of this experimental work.

References

1. Bailliet H, Lotton P, Bruneau M, Gusev V, Valiere JC, Gazenbel B (2000) Acoustic power flow measurement in a thermoacoustic resonator by means of laser Doppler anemometry (LDA) and microphonic measurement. Appl Acoust 60(1):1–11
2. Berson A, Blanc-Benon P, Michard M (2006) Ecoulements secondaires aux extrémités du stack d'un réfrigérateur thermoacoustique : mesure des champs de vitesse oscillante à l'aide de la PIV. In: 8ème Congrès Français d'Acoustique (CD-ROM), Tours, pp 749–752
3. Besnoin E, Knio OM (2004) Numerical study of thermoacoustic heat exchangers. Acta Acust United Acust 90:432–444
4. Biwa T, Ueda Y, Yazaki T, Mizutani U (2001) Work flow measurements in a thermoacoustic engine. Cryogenics 41(5):305–310
5. Blanc-Benon P, Marx D (2005) Nonlinear effects in standing wave thermoacoustic resonator. In: First joint workshop of Russian Acoustical Society (RAS) and French Acoustical Society (SFA) on "High intensity acoustic waves in modern technological and medical applications", special session of the XVI Meeting of the RAS, Moscow, pp 57–65
6. Blanc-Benon P, Besnoin E, Knio OM (2003) Experimental and computational visualization of the flow field in a thermoacoustic stack. CR Mécanique 331:17–24
7. Campbell M, Cosgrove JA, Greated CA, Jack S, Rockliff D (2000) Review of LDA and PIV applied to the measurement of sound and acoustic streaming. Opt Laser Technol 32:629–639
8. Cao N, Olson JR, Swift GW, Chen S (1996) Energy flux density in a thermoacoustic couple. J Acoust Soc Am 99(6):3456–3464
9. Duffourd S (2001) Réfrigérateur thermoacoustique : études analytiques et expérimentales en vue d'une miniaturisation 2001–06. PhD thesis, Ecole Centrale de Lyon
10. Graftieaux L, Michard M, Grosjean N (2001) Combining PIV, POD and vortex identification algorithms for the study of unsteady turbulent swirling flows. Meas Sci Technol 12:1422–1429
11. Hann DB, Greated CA (1997) Particle image velocimetry fort the measurement of mean and acoustic particle velocities. Meas Sci Technol 8:656–660
12. Herman C, Kang E, Wetzel M (1998) Expanding the applications of holographic interferometry to the quantitative visualization of oscillatory thermofluid processes using temperature as tracer. Exp Fluids 24:431–446
13. Humphreys WM, Bartram SM, Parrott TL, Jones MG (1998) Digital PIV measurements of acoustic particle displacements in a normal incidence impedance tube. In: 20th AIAA advanced measurement and ground testing technology Conference, Albuquerque
14. Ishikawa H, Mee DJ (2002) Numerical investigations of flow and energy fields near a thermoacoustic couple. J Acoust Soc Am 111(2):831–839
15. Marx D (2003) Simulation numérique d'un réfrigérateur thermoacoustique 2003–34. PhD thesis, Ecole Centrale de Lyon
16. Marx D, Blanc-Benon P (2003) Numerical simulation of hydrodynamic and thermal effects around a 2-D stack plate in a thermoacoustic refrigerator. J Acoust Soc Am 114(4):2329
17. Marx D, Blanc-Benon P (2004) Numerical simulation of stack-heat exchangers coupling in a thermoacoustic refrigerator. AIAA J 42(7):1338–1347
18. Marx D, Blanc-Benon P (2005) Computation of the temperature distortion in the stack of a standing-wave thermoacoustic refrigerator. J Acoust Soc Am 118(5):2993–2999
19. Melling A (1997) Tracer particles and seeding for particle image velocimetry. Meas Sci Technol 8:1406–1416
20. Merkli P, Thomann H (1975) Transition to turbulence in oscillating pipe flow. J Fluid Mech 68(3):567–575
21. Paek I, Braun JE, Mongeau L (2005a) Characterizing heat transfer coefficients for heat exchangers in standing wave thermoacoustic coolers. J Acoust Soc Am 118(4):2271–2280
22. Paek I, Braun JE,Mongeau L (2005b) Second law performance of thermoacoustic systems. J Acoust Soc Am 118(3):1892
23. Poese ME, Garrett SL (2000) Performance measurements on a thermoacoustic refrigerator driven at high amplitudes. J Acoust Soc Am 107(5):2480–2486
24. Rott N (1980) Thermoacoustics. Adv Appl Mech 20:135–175
25. Swift GW (1988) Thermoacoustic engines. J Acoust Soc Am 84(4):1145–1180
26. Taylor KJ (1976) Absolute measurement of acoustic particle velocity. J Acoust Soc Am 59(3):691–694
27. Thompson MW, Atchley AA (2005) Simultaneous measurement of acoustic and streaming velocities in a standing wave using laser Doppler anemometry. J Acoust Soc Am 117(4):1828–1838
28. Wetzel M, Herman C (2000) Experimental study of thermoacoustic effects on a single plate part I: temperature fields. Heat Mass Transf 36:7–20
29. Wetzel M, Herman C (1997) Design optimization of thermoacoustic refrigerators. Int J Refrig 20(1):3–21
30. Worlikar A, Knio O (1996) Numerical simulation of a thermoacoustic refrigerator. J Comput Phys 127:424–451